Automatic Segmentation of the Left Ventricle Cavity and Myocardium in MRI Data

M. Lynch *, O. Ghita P. F. Whelan

Vision Systems Group, Dublin City University, Dublin 9, Ireland

Abstract

A novel approach for the automatic segmentation has been developed to extract the contours of the *epi-cardium* and *endo-cardium* boundary of the left ventricle of the heart. The developed segmentation scheme takes multi-slice and multi-phase Magnetic Resonance (MR) images of the heart, transversing the short-axis length from the base to the apex. Each image is taken at one instance in the heart's phase. The images are segmented using a diffusion-based filter followed by an unsupervised clustering technique and the resulting labels are checked to locate the left ventricle (*lv*) cavity. From cardiac anatomy, the closest pool of blood to the *lv* cavity is the right ventricle cavity. The wall between these two blood-pools (*interventricular septum*) is measured to give an approximate thickness for the myocardium. This value is used when a radial search is performed on a gradient image to find appropriate robust segments of the epi-cardium boundary. The robust edge segments are then joined using a normal spline curve. Experimental results are presented with very encouraging qualitative and quantitative results and a comparison is made against the state-of-the art level-sets method.

Preprint submitted to Elsevier Science *6 October 2004*

Key words: MRI, left ventricle, segmentation, myocardium, clustering, level-set

1 Introduction

According to the World Health Organisations [1] 2002 Report, 29% of deaths in their 191 members states were a result of cardiovascular disease (CVD), 32% in women and 27% in men. These alarming statistics have spurred the increase in research into the diagnosis and prevention of CVDs. The size and structure of the left ventricle is a primary indicator for the diagnosis and treatment monitoring of many CVDs. For example, left ventricle contraction and thickening plays a key role in the assessment of deficient blood supply to the cardiac tissue (ischaemia) [2] while a fall in left ventricle output or the ejection fraction can be a late complication of elevated vascular resistance (hypertension). Diagnostic imaging is set to play a vital role in the future fight against heart disease.

Traditional methods of cardiac imaging include cardiac ultrasound and angiography. Cardiac ultrasound is a tomographic imaging system, it is relatively cheap, non-invasive and can image on arbitrary planes. It gives low contrast when compared to MR and X-ray and hence cannot image through gaseous mediums and has a low signal-to-noise (SNR) ratio due to frequency attenuation in the tissue. Also, it has a low SNR in cases where the patient presents obesity. 3D ultrasound [3,4] has been introduced to analyse the heart function

* Corresponding author.
Email address: lynchm@eeng.dcu.ie (M. Lynch).

but currently does not have the resolution to accurately distinguish between the epi-cardium border and other organs in the thoracic cavity [5].

In angiography, X-ray projection images are used. The quality of the image can suffer when the heart muscle is overlapped by the diaphram or the ribs. A contrast agent is injected into the heart cavity by means of a pigtail catheritor threaded through the arteries. This may cause complications like *arrhythmias* (irregular heartbeat) or *embolism* (by dislodging plaque from the wall) and may even result in death. This contrast agent also has difficulty reaching the apex of the heart [6].

Cardiac Magnetic Resonance Imaging (CMRI), which is used in this study is a well established and rapidly advancing imaging modality in analysing heart disease. It is considered by some authors [7,8] to be the reference standard. MR has proved to be more accurate than echo-cardiology in the calculation of the ejection fraction and also shown superior results in endo-cardium border segmentation [8]. It has a wide topographical field of view and high contrast between soft tissues without the need for a contrast agent. This means there is a high discrimination between the flowing blood and the myocardium muscle. It is non-invasive with high spatial resolution and can be gated using an *electrocardiogram* (ECG) at different phases during the hearts pulse. However, it can suffer from noise and gray scale variation between adjacent slices [6,9–13].

All of these modalities are providing increasing amounts of information in higher dimensions, spatially and temporally. Such an increase in data pro-

duced from the different modalities makes it much more laborious and time-consuming for the cardiologist to hand-annotate and measure the myocardium. Recent research projects have moved from a manual segmentation toward a fully automated segmentation of the left ventricle [14–16,9].

1.1 Segmentation Background

Computer Aided Diagnostic (CAD) tools have been developed to aid cardiologists with the manual delinearisation of the myocardium [17,18]. Measurements are taken using geometric approximations of the left ventricle (lv). While these geometric models are fair approximations for healthy patients, they are not as accurate when compared to the actual MR image data [7]. Manual segmentation also suffers from inter- and intra- observer variability.

Semi-automated methods have been developed in order to further aid the cardiologist in the segmentation process [19–21]. These methods require user intervention by placing an initial contour around the lv or moving the cursor around the lv wall while the border attaches itself to the high gradient points. Although these approaches considerably reduce the time taken to manually segment the myocardium boundary it is still subject to inter- and intra-observer variability.

Traditional methods of segmentation such as thresholding, region-growing, edge-detection and watershed [22–24] (reviewed in [6]) are also used in the evaluation of the left ventricle cavity and wall. These methods on their own

have difficulty dealing with noise, gray scale variations and low gradients associated with most medical images and a high degree of supervision is required from the user.

Snakes or active contours [25] are curves that move toward the sought-for shape in a way that is controlled by internal forces such as rigidity, elasticity, and an external image force. The external force should attract the contour to certain features, such as edges in the image [26–29]. Initialisation of the contour is the key to its success. Bad initialisation can draw the curve away from the left ventricle to edges that best fit its predefined parameters. Snakes and active contours have difficulty working on images with low contrast and may not be able to flag important features such as wall thinning.

Level-set [30] methods have become well established methods for segmentation. Level-sets have also become a prevalent method in medical image segmentation [31–33]. Level-sets have gained popularity due to their implicit nature and ability to perform well in noisy data. They also have the ability to split and re-join throughout the deformation without the need for re-parameterisation. Similar to active contours, they rely on the first initialisation step and can fall into the trap of local minima.

Recently, in the field of medical image processing, many model-based segmentation approaches have been studied (reviewed in [10,34]). Geometrically deformable models [35–37] are parametric representations of the desired shape to be segmented. These parametric models can enhance the local properties of

an image such as gray level or texture to aid the delinerisation in poor quality images.

Active shape models (ASMs) [38–40] are a model driven segmentation approach. The model is built up using *a priori* knowledge about the left ventricle shape, usually hand-annotated segmentations from a training set of data. This shape model is then compressed, usually using principle component analysis (PCA), to find the common modes of shape variation. The mean shape then searches an unseen image and converges over the most likely set of features. The mean shape is then deformed using the PCA modes. The accuracy of the segmentation relies heavily on the amount and variation of images in the training set. If the training set is too small with low variation, there is a limited number of unseen images that the model is applicable too. On the other hand, if the model is large with large variation it may easily choose some erroneous points. The hand annotation of the training set can also be very time consuming and introduce bias.

Active appearance models (AAM) [38,16] are similar to ASMs but texture of the shape is added to the model and they perform a combined shape-appearance statistical analysis. Stegmann [41] showed how these active appearance models could be applied to analyse short axis MR images of the heart. Mitchell [42] addresses the problems that AAMs have with attaching the model with the gradient information by formulating a hybrid approach which combines ASMs and AAMs. Lelieveldt [43] introduces a time factor into his Active Appearance Motion Models and minimises the appearance-to-target differences. Again all AAMs suffers the same limitations as the shape

models with regards to the variation and building of the training sets.

We present a two-phase approach to address these issues. A diagram for the segmentation scheme is illustrated in figure 4. In the first stage automatically locates and segments the *lv* cavity. It is invariant to changes in scale and changes in gray scale through the volume image. It performs a true segmentation of the endo-cardium boundary including the papillary muscles attached to the myocardium. The inclusion or exclusion of the papillary muscles in the calculation of the ejection fraction is usually dependent on the radiologist who can make this decision once the automatic segmentation is performed. In the second phase, we use the thickness of the interventricular septum (the myocardium between the left and right ventricle) as a guide for segmenting the remainder of the epi-cardium, using edge information. The epi-cardium boundary is closed using a spline.

This paper is organised as follows: Section 2 discusses the preprocessing with a short description of the segmentation algorithm. Section 3 focuses on the automatic detection of the *lv* cavity where we perform the segmentation of the *lv* cavity on both the end-systole and end-diastole phases and calculate the ejection fraction subsequently [44]. Section 4 moves onto the heuristics involved in segmenting the outer wall of the myocardium. The results are shown and evaluated in Section 5 with concluding remarks in Section 6.

2 Smoothing and Clustering algorithms in brief

Each image slice is smoothed to remove the noise which occurs in MR images [23]. The image is then clustered using an adapted k-means algorithm. The clustering of MRI data using different clustering techniques has being documented in [45,46].

2.1 Edge-preserving Smoothing

In this preprocessing step, noise is filtered out of the image while maintaining the important edge information using an edge preserving filter. The use of diffusion-based filters also been performed in MRI data [47–50] . The adaptive smoothing algorithm proposed by Chen [51] is an adaptation of [52] but searches the image for both local and contextual discontinuities. These discontinuities are preserved during the smoothing operation.

2.1.1 Local Discontinuities

The local discontinuity is measured using four detectors:

$$\begin{aligned} E_{H_{xy}} &= |I_{x+1,y} - I_{x-1,y}|, \\ E_{V_{xy}} &= |I_{x,y+1} - I_{x,y-1}|, \\ E_{D_{xy}} &= |I_{x+1,y+1} - I_{x-1,y-1}|, \\ E_{C_{xy}} &= |I_{x+1,y-1} - I_{x-1,y+1}| \end{aligned} \tag{1}$$

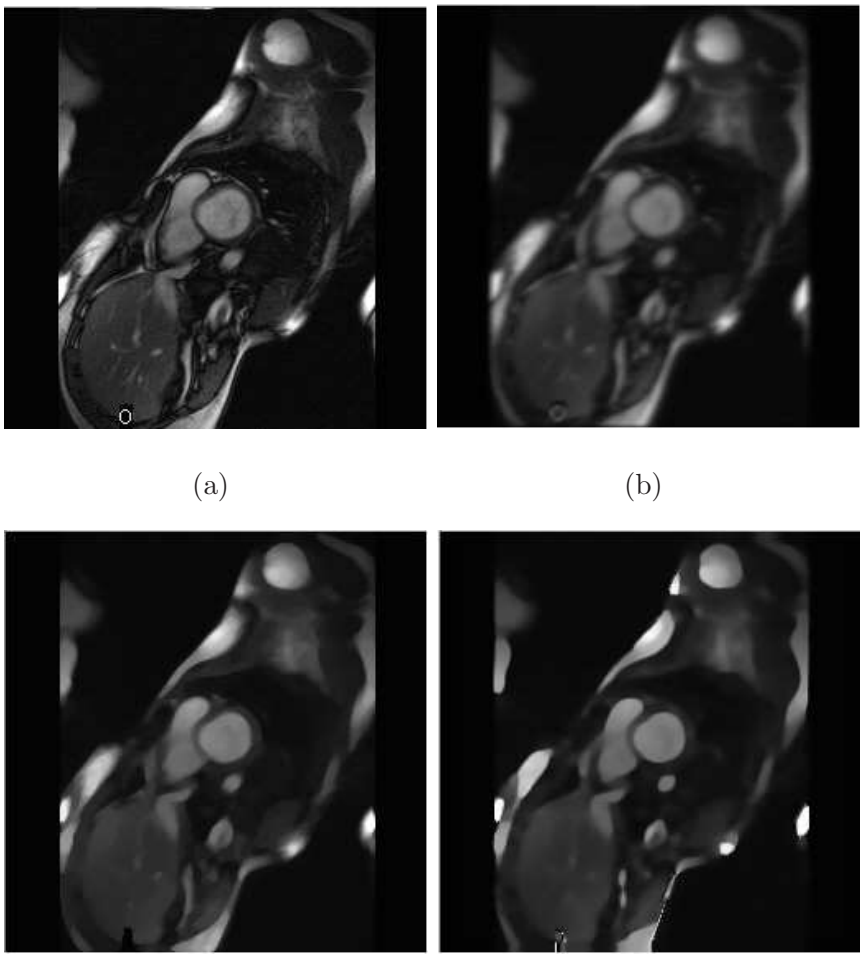

(a) (b)

(c) (d)

Fig. 1. Figures show the filtering of the short axis view *(a)* The original image of the short axis view *(b)* Results after a single pass of a 5x5 average filter, *(c)* Shows the results after a single pass of a 5x5 fifth-largest median filter and *(d)* The results from the Adaptive filtering using a 5x5 neighbourhood mask, note the preservation of the edge features.

where $I_{x,y}$ is the gray scale value of the image at position (x, y). The local discontinuity measure at that point can then be defined as:

$$E_{xy} = \frac{E_{H_{xy}} + E_{V_{xy}} + E_{D_{xy}} + E_{C_{xy}}}{4} \tag{2}$$

2.1.2 Contextual Discontinuities

The contextual discontinuities are then measured using the spatial variance. A square kernel $N_{xy}(R)$ is first set up and the mean of its members calculated:

$$\mu_{xy}(R) = \frac{\sum_{(i,j)\in N_{xy}(R)} I_{i,j}}{|N_{xy}(R)|} \tag{3}$$

The spatial variance is then calculated to be:

$$\sigma^2_{xy}(R) = \frac{\sum_{(i,j)\in N_{xy}(R)} (I_{i,j} - \mu_{xy}(R))^2}{|N_{xy}(R)|} \tag{4}$$

This variance is then normalised to $\tilde{\sigma}^2_{xy}$ and thresholded with $\theta_\sigma = (0 \leq \theta_\sigma \leq 1)$ to limit the number of contextual discontinuities.

2.1.3 Smoothing Algorithm

Using two forms of discontinuities above leads to a less ambiguous smoothing solution, the local discontinuities indicate detailed local structures and the contextual discontinuities show important features. The algorithm is iterative and the updated pixel values now become:

$$I^{t+1}_{xy} = I^t_{xy} + \eta_{xy} \frac{\Sigma_{(i,j)\in N_{xy}(1)/\{(x,y)\}} \eta_{ij} \gamma^t_{ij} (I^t_{i,j} - I^t_{x,y})}{\Sigma_{(i,j)\in N_{xy}(1)/\{(x,y)\}} \eta_{ij} \gamma^t_{ij}} \tag{5}$$

where,

$$\eta_{ij} = \exp(-\alpha \Phi(\tilde{\sigma}^2_{xy}(R), \theta_\sigma)), \tag{6}$$

$$\gamma^t_{ij} = \exp(-E^t_{ij}/S) \tag{7}$$

The variables S and α determine the extent to which the local and contextual discontinuities should be preserved during smoothing. If there are a number of contextual discontinuities in the image then the value of η_{ij} will have a large

influence on the updated intensity value. On the other hand, if there are a number of local discontinuities, then both γ_{ij} and η_{ij} will have the overriding effect, as η_{ij} is used for gain control of the adaption [51]. The values used in the smoothing were a window size of $R = 1$ (this translates to a 3x3 smoothing window), run for 3 iterations, $\theta_\sigma = 0.2$, $S = 10.0$ and $\alpha = 10$. These values were found experimentally to give the optimal results for all the images used in this study.

2.2 Clustering

The smoothed images are then clustered using an adaptation of the k-means algorithm proposed by Duda and Hart [53,54]. This algorithm has four steps to find the image clusters.

(i) Initialise the position of the means $m_1 \rightarrow m_k$.

(ii) Assign each of the k-items to the cluster whose mean is nearest.

(iii) Recalculate the mean for the cluster gaining the new item and the mean for the cluster loosing the same item. Recalculation is made using the variance.

(iv) Loop through steps *(ii)* and *(iii)* until there are no movements of items.

The image is clustered using an initial guess of 15-20 independent cluster centres which is sufficient to capture all the relevant features. The pixels are clustered together using the strategy explained before. The number of clusters is then optimised by merging clusters with similar attributes. This is repeated until there are no more clusters to be merged [44].

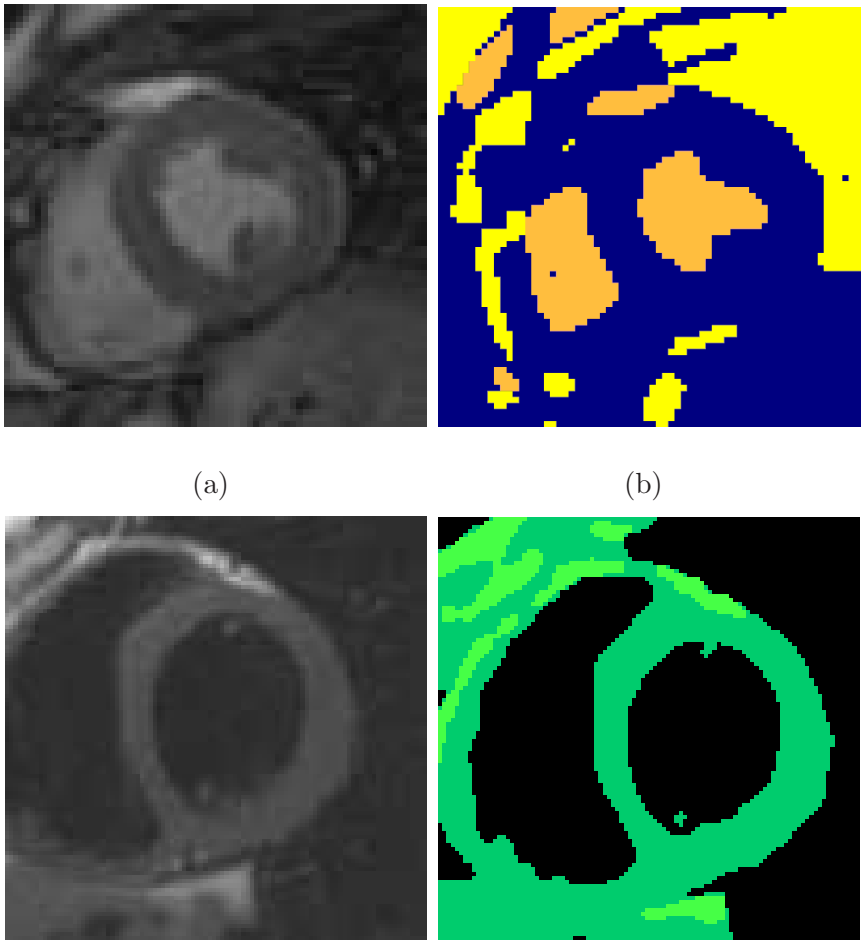

(a) (b)

(c) (d)

Fig. 2. Figure shows four images, two gradient-echo images before (a) and after clustering (b), and two spin-echo images before (c) and after clustering (d).

3 Automatic Detection of *lv* cavity

The image has now been segmented into separate clustered regions. The next step is to automatically detect which of these clusters represents the *lv* cavity on the first slice. To allow for different imaging parameters the *lv* cavity is located using shape descriptors only and not using the gray scale values. The images are short axis, therefore we assume that the *lv* cavity approximates a circular shape and that the *lv* feature is continuous in successive slices. Approximation to a circle is calculated as the error between the shape and the

least squares approximation to the circle (see *Appendix*). It is also assumed that the *lv* is not located on the peripheral of the image.

The volume of the left ventricle is then extracted using two criteria:

(i) Overlapping area of the regions contained in successive slices.

(ii) Gray scale value of the regions under investigation

The regions cannot be connected using just gray scale values due to the variation in the intensity values through the volume caused, to some extent, by coil intensity falloff. The *lv* regions are then connected in 3D and the volumes are then rendered (see figure 3). The ejection fraction is calculated using the volumes. The ejection fraction is defined as "the proportion, or fraction, of blood pumped out of your heart with each beat" [55] and can be represented by the equation:

$$EF = \frac{V_{endo}(t_D) - V_{endo}(t_S)}{V_{endo}(t_D)} \tag{8}$$

where V_{endo} is the volume of the inner walls of the heart, $V_{endo}(t_D) = max_t[V_{endo}(t)]$ is the end-diastolic volume and $V_{endo}(t_S) = min_t[V_{endo}(t)]$ is the end-systolic volume.

4 Segmentation of epi-cardium border

The procedure for segmenting the epi-cardium is illustrated in figure 4. The position of the *lv* cavity is already known for each slice as explained in the previous section. In order to determine the epi-cardium border a region of

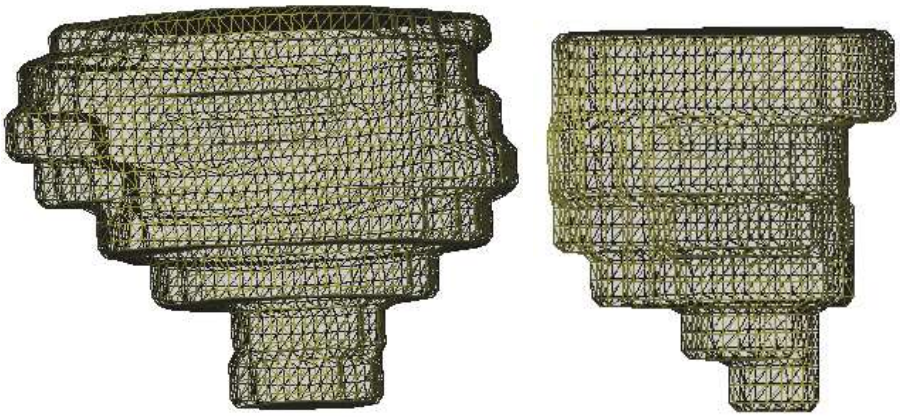

(a) (b)

Fig. 3. The rendered images of the *(a)* end-diastole and the *(b)* end-systole phases of the cardiac cycle. These volumes that are constructed from the true segmentation of the images excluding fat and papillary muscles on the endo-cardium.

interest is defined around the *lv* cavity. Two copies of this region of interest are taken. The first image $Image1$ is used to find a value for the approximate radius of the myocardium and the second image $Image2$ is used to find real borders around the myocardium. The two are combined to find the true value of the epi-cardium around the *lv*.

$Image1$ is again clustered using a predefined low number of clusters around the region of interest. A low number of clusters is chosen because of the scarcity of important features around the *lv* cavity. Anatomically, the closest blood pocket to the *lv* cavity is the right ventricle cavity, it is also known that the thickness of the myocardium will not change drastically over the entire circumference. The thickness of the *interventricular septum* between the two blood pockets can give a reliable estimate for the thickness of the rest of the myocardium.

$Image2$ is zoomed using an area averaging technique around the area of interest. The zooming operation is applied to increase the edge separation. The image is then segmented using a thresholded edge-based algorithm [56]. The largest connected segments within certain bounds of the estimated thickness found from $Image1$ are taken as potential border segments. There is an angular restraint placed on the transition of these segments around the epi-cardium to eliminate stepping into the endo-cardium border or stepping out to other organs.

A closed natural cubic spline is fitted around the points on the epi-cardium [57] (see *Appendix*). The spline is used to close the epi-cardium contour by connecting all the points on the curve in a smooth way. Splines are piecewise polynomials of degree n ($n = 3$ in the case of cubic splines) with the pieces smoothly joined together. The joining points of the polynomial pieces are called control points which need not be evenly spaced.

5 Results

In order to assess the performance of the automatic segmentation, results were compared against those obtained by manually segmenting 25 volume image sequences for the endo- and epi-cardium borders. The manual segmentation was assisted by an experienced cardiologist. Each volume includes 5-12 images containing the *lv*, transversing the lenght of the cavity and includes the papillary muscles. The imaging device used was a Siemens Magnetom Sonata, 1.5 Tesla, TR = $3.2ms$, TE = $1.6ms$, flip-angle 60° and resolution $(1.37 \times 1.37 \times 8mm)$ for the bright blood sequence and a Siemens Vision $1.5T$, T1-weighted scan

used in the dark blood sequence. The automatic segmentation results can be seen in figure 5. The method shows good visual results for bright blood images 5(a)-(f) and dark blood images 5(g)-(i). The errors are calculated on volumes, endo and epi contours areas, myocardium thickness and finally point correspondence. The latter is measured against a level-set segmentation (see *Appendix*).

Table 1 shows the signed average and root mean square error of the ejection fraction from eight volumes from the sequence. The ejection fractions were worked out using pairs of volumes, not necessarily the end-systole and end-diastole and compared with the ejection fraction calculated from the manually segmented volumes. We can see in Table 1 low errors between the manual and automatic results.

The errors for the manually segmented endo-cardium area and the automatically traced area are given in Table 1. The signed average and root mean square error are shown. Errors around the apex have a significant effect because a low number of pixels is a high proportion of the overall manually traced area. Linear regression analysis was also performed in figure 7(a) and high correlation value of $r = 0.98$ is obtained. Reproducibility is assessed using the Bland-Altman plot, figure 7(c) [58]. Note that the graphs are relatively zoomed to show the detailed distribution and the plots are graphed in units of mm^2.

The epi-cardium area was assessed using the same techniques. It shows a

slightly lower percentage error for both the average signed and the rms errors. This can be attributed to the increased overall area of the manually traced contours. Linear analysis, figure 7(b), gives an value of $r = 0.94$ which is slightly lower than that produced for the endo-cardium. This lower correlation is a result of low contrast on the lateral side of the heart making the segmentation of the epi-cardium border difficult. In this case our algorithm connects two end-points of robust segments, how the ends are connected can incorporate *a priori* information [59]. Manual segmentation is also problematic in areas of low gradient and is dependent on the the users own interpretation of 'what looks appropriate'. Reproducibility was again assessed with the Bland-Altman plot, figure 7(d).

Tables 2 and figure 8 gives the Euclidean point to curve error in mm's for >150 images through a heart sequence. It gives the minimum and maximum distance between the manual and automatic segmentation contours. The average distance, standard deviation (SD) and root-mean-square (RMS) are also given. The results are compared to those obtained using the level set technique, detailed in the *Appendix* , where the user selects the *lv* cavity for each image. The large maximum errors taken from the level-set approach are mainly due to the level-set encountering local minima due to the variation in blood intensity in the image. The results for the epi-cardium boundary point to curve errors are shown in Table 3 and illustrated in figure 9.

Table 1

Mean Percentage Errors ± 1SD for manual versus automatic

	Average Signed Error	RMS Error
Ejection Fraction	1.593 ± 0.82	3.176
Endocardium Areas	-3.623 ± 5.14	4.765
Epicardium Areas	-0.556 ± 4.29	3.75

Table 2

Point to curve Errors between manual and computer segmentation for both the clustering and level-set techniques for the endo-cardium boundary(*mm*)

	Endo				
Method	*Min (mm)*	*Max (mm)*	*Average (mm)*	*SD (mm)*	*RMS (mm)*
Clustered	0.0	7.07	0.69	0.88	1.12
Level-Set	0.0	10.296	1.08	1.36	1.73

Table 3

Point to curve Errors between manual and automatic segmentation for the epi-cardium boundary(*mm*)

	Endo				
Method	*Min (mm)*	*Max (mm)*	*Average (mm)*	*SD (mm)*	*RMS (mm)*
Robust Arc	0.0	13.45	1.31	1.86	2.14

6 Conclusion

A fully automatic detection and segmentation of the left ventricle myocardium has been detailed in this paper. An edge preserving filter followed by an unsupervised clustering to successfully segment the left ventricle cavity from short axis MR images of the heart. Once the cavity volume is extracted the ejection

fraction can be calculated. The edge-point accuracy is compared with level-set segmentation of the blood pool.

In the second part of the paper the epi-cardium border is successfully segmented using an edge-based technique. The thickness of the wall is approximated by measuring the thickness of the interventricular septum. The interventricular septum is an anatomically sound feature of the heart and because it is surrounded by blood on both sides it can be robustly segmented. This measurement is then used as an initial estimate for the thickness of the complete wall. A gradient image of the area around the *lv* is computed and the use of the approximate wall thickness, gradient points potentially belonging to the epi-cardium border are selected. If there are no viable gradients found on the epi-cardium border then the outer wall is estimated using the approximation found using the interventricular septum.

We believe that general models in ASMs\AAMs built up from training sets are limited in their application to the variety of heart shapes. Abnormalities in the image data can indicate disease. Model based approaches approximate to the closest plausible instance shape from the training set Point Distribution Model (PDM), but this may not be sufficiently accurate. Also AAMs cannot deal well with the changes in texture. This paper presents a robust, fully automated method to identify the endo-cardium and epi-cardium borders that does not rely on *a priori* knowledge nor does it use constraints to find the left ventricle cavity.

Left ventricle segmentation is primarily motivated by the need to clinically

diagnose a feature of the heart with potential problems. Models that approximate left ventricular boundaries try to fit variations of boundaries that have already been segmented. The left ventricle is anatomically variant, the scanners are inconsistant and the variations of pathologies found in patients is vast. To build a model to accommodate such diversity would be an immense task. Our algorithm makes no approximations but produces a true evaluation of the heart structure by segmenting the true borders in the image. We should remember that the aim is not to segment hearts that are part of a model but to assist the cardiologist in the prognosis by delineating the true anatomical features present in the image.

Evaluating the endo-cardium and epi-cardium borders using this approach could provide a more appropriate technique for flagging problems like wall thinning and low ejection fraction.

Acknowledgments

Many thanks to Rob van der Geest, Department of Radiology, Leiden University whose help was gratefully appreciated. He also generously supplied gradient-echo DICOM sequences shown in this paper courtesy of Cory Swingen, University of Minnesota, Minneapolis. The authors would also like to thank Dr. John Murray, Mater Misericordiae Hospital, Dublin, Ireland for his advice on segmentation and assessing the value of this paper from a medical point of view.

Appendix

LMS Circle

Using the Least Squares solution a circle is fitted around a collection of points, P_i, with images coordinates, (x_i, y_i) for $i = 1, 2...N$.

A circle is defined by three parameters. These parameters are the coordinates of its centre (x_0, y_0) and its radius r. The equation of a circle can be written isolating these three parameters as follows:

$$\begin{pmatrix} 2x_i & 2y_i & 1 \end{pmatrix} \begin{pmatrix} x_0 \\ y_0 \\ r^2 - x_0^2 - y_0^2 \end{pmatrix} = \begin{pmatrix} x_i^2 + y_i^2 \end{pmatrix}$$

In order to find these three unknowns a linear least squares solution is obtained where:

$$A = \begin{pmatrix} 2x_1 & 2y_1 & 1 \\ 2x_2 & 2y_2 & 1 \\ 2x_3 & 2y_3 & 1 \\ & ... & \\ 2x_N & 2y_N & 1 \end{pmatrix} \quad , b = \begin{pmatrix} x_1^2 + y_1^2 \\ x_2^2 + y_2^2 \\ x_3^2 + y_3^2 \\ ... \\ x_N^2 + y_N^2 \end{pmatrix}$$

The best fitting circle for the points P_i is the least squares solution to $[x_0 \quad y_0 \quad r^2 -$

$x_0^2 - y_0^2]^T = (A^T A)^{-1} A^T b$ where $(A^T A)^{-1} A^T b$ can be written as:

$$\begin{pmatrix} 4\sum x_i^2 & 4\sum x_i y_i & 2\sum x_i \\ 4\sum x_i y_i & 4\sum y_i^2 & 2\sum y_i \\ 2\sum x_i & 2\sum y_i & N \end{pmatrix}^{-1} \begin{pmatrix} 2\sum x_i^3 + 2\sum x_i y_i^2 \\ 2\sum y_i^3 + 2\sum x_i^2 y_i \\ \sum x_i + \sum y_i^2 \end{pmatrix}$$

The errors of this least squares solution can be calculated with $e_{circle} = \| A[x_0 \quad y_0 \quad r^2 - x_0^2 - y_0^2] - b \|$

Splines

A spline fits a smoothed curve around a collection of points P_i where $i = 1, 2, 3...N$. It works by fitting a cubic curve between each pair of points in the collection. Smoothness of the curve is maintained by forcing the first and second derivative of the end point of one curve to equal the start of the next curve. This is achieved by solving a system of simultaneous equations. The equation is illustrated below:

$$f_i(x) = a_i + b_i u + c_i u^2 + d_i u^3$$

$$0 \leq u \leq 1$$

$$1 \leq i \leq n$$

Where i is the amount of points on the curve and u is the number of steps in between each point. The coefficients of the cubic equation are:

$$
\begin{aligned}
a &= x_n \\
b &= \frac{dx_n}{dP} \\
c &= 3(x_{n+1} - x_n) - 2\frac{dx_n}{dP} - \frac{dx_{n+1}}{dP} \\
d &= 2(x_n - x_{n+1}) + \frac{dx_n}{dP} + \frac{dx_{n+1}}{dP}
\end{aligned}
$$

The derivatives used in to smooth the curve are computed as follows:

$$
\begin{pmatrix} \\ D[0] \\ \\ D[1] \\ \\ . \\ \\ . \\ \\ . \\ \\ D[n] \\ \\ \end{pmatrix}
=
\begin{pmatrix}
 & & & & & & \\
4 & 1 & & & & & 1 \\
1 & 4 & 1 & & & & \\
 & 1 & 4 & 1 & & & \\
 & & \ldots & & & & \\
 & & & & 1 & 4 & 1 \\
1 & & & & & 1 & 4
\end{pmatrix}^{-1}
\begin{pmatrix} \\ 3(x_1 - x_n) \\ \\ 3(x_2 - x_0 \\ \\ . \\ \\ . \\ \\ 3(x_n - x_{n-2} \\ \\ 3(x_0 - x_{n-1}) \\ \\ \end{pmatrix}
$$

Level-Set Formulation

The formulation of the problem is straight forward. The evolving curve or front Γ, evolves as the zero level-set of a higher dimensional function ϕ. This function deforms with a force F that is dependent on both curvature of the front and external forces in the image. The force acts in the direction of the normal to the front.

$$
\begin{aligned}
\phi_t + F|\nabla\phi| &= 0 \\
\phi(x, y, t = 0) &= given
\end{aligned}
\tag{9}
$$

Our implementation is a standard two step approach which includes a fast-marching initial step to speed up the segmentation. Fast marching is a special case of the above equation where $F(x, y) > 0$. Let $T(x, y)$ be the time that the front Γ crosses the point (x, y). The function $T(x, y)$ then satisfies the equation;

$$|\nabla T|F = 1 \tag{10}$$

which simply says that the gradient of the arrival time is inversely proportional to the speed of the surface. The T function is evaluated using the diffusion and attraction to pixels within the front. The front grows out from its initial position to points with the smallest value of $T(x, y)$. The $T(x, y)$ function is then updated and and continued until the front does not grow.

The fast-marching step is then followed with a fine tuning step using a narrow-band level-set method. Here the shape model is implicitly represented as the zero level-set of a function ϕ. Where ϕ = signed distance to the Γ, negative if inside the front and positive if outside. ϕ is iteratively updated as;

$$\phi_{t+1} = \phi_t + k_I(1 - \epsilon\kappa)|\nabla\phi| + \beta\nabla I \cdot \nabla\phi \tag{11}$$

where ϵ and *beta* are user parameters, κ is the curvature term and equal to $\nabla \cdot \frac{\nabla\phi}{|\nabla\phi|}$ and k_I is an image dependent speed term and is given by $\frac{1}{1+\nabla I}$. The third term, $\nabla I \cdot \nabla\phi$ represents the attractive force vector normal to the front. The updates were performed efficiently within a narrow-band around the front.

Authors

Michael Lynch received his B.Eng.(Hons) degree in Mechatronic Engineering from Dublin City University, Dublin, Ireland in 2002. He joined the Vision Systems Group in Dublin City University at the start of 2003 as a research student working towards an Ph.D. Current research interests include image processing and medical imaging, with emphasis on cardiac imaging. He is also a student member of the IEEE, SPIE and IAPR.

Ovidiu Ghita received his B.E. and M.E. degrees in Electrical Engineering from Transilvania University, Brasov, Romania. From 1994 through 1996 he was an Assistant Lecturer in the Department of Electrical Engineering at Transilvania University. Since then, he has been a member of the Vision Systems Group at Dublin City University (DCU), during which time he received his Ph.D. for work in the area of robotic vision. Currently, he holds the position of Post-doctoral Research Assistant in the Vision Systems Laboratory at DCU. His current research interests are in the area of machine learning, shape representation and medical imaging.

Paul F Whelan received his B.Eng.(Hons) degree from the National Institute for Higher Education Dublin, a M.Eng. degree from the University of Limerick, and his Ph.D. in computer vision from the University of Wales, Cardiff (UK). Having begun his research career in industry, he joined the Faculty of Engineering and Design at Dublin City University (DCU) in 1990. He currently holds the position of Associate Professor and is the founding Director

of the Vision Systems Group in DCU.

As well as a wide range of scientific publications, Prof. Whelan co-edited *Selected Papers on Industrial Machine Vision Systems* (1994), and was the co-author of *Intelligent Vision Systems for Industry* (1997) and *Machine Vision Algorithms in Java* (2000). His research interests include applied morphology, texture analysis with a specific focus on applications in machine vision and medical imaging. He is a Senior Member of the IEEE, a Chartered Engineer and a member of the IEE and IAPR. He currently serves as member of the governing board of the *International Association for Pattern Recognition* (IAPR) and as the President of the *Irish Pattern Recognition and Classification Society.*

References

[1] A. Rodgers, P. Vaughan, The World Health Report 2002, Reducing risks, promoting healthy life, The World Health Organisation, 1211 Geneva 27, Switzerland (2002).

[2] H. Azhari, S. Sideman, J. L. Weiss, E. P. Shapiro, M. L. Weisfeldt, W. L. Graves, W. J. Rogers, R. Beyar, Three-dimensional mapping of acute ischemic regions using MRI: wall thickening versus motion analysis, AJP - Heart and Circulatory Physiology 259 (5) (1990) 1492–1503.

[3] H. A. McCann, J. C. Sharp, T. M. Kinter, C. N. McEwan, C. Barillot, J. F. Greenleaf, Multidimensional Ultrasonic Imaging for Cardiology, Proceedings of the IEEE 76 (9) (1988) 1063–1073.

[4] G. Sanchez-Ortiz, J. Declerk, M. Mulet-Parada, et al., Automating 3D Echocardiographic Image Analysis, in: Proceedings of MICCAI 2000, Pittsburg, PA, USA, 2000, pp. 687–696.

[5] M. D. Cerqueira, N. J. Weissman, V. Dilsizian, A. K. Jacobs, S. Kaul, W. K. Laskey, D. J. Pennell, J. A. Rumberger, T. Ryan, M. S. Verani, Standardized Myocardial Segmentation and Nomenclature for Tomographic Imaging of the Heart, American Heart Association Writing Group on Myocardial Segmentation and Registration for Cardiac Imaging 105 (2002) 539–542.

[6] J. S. Suri, S. K. Setarehdan, S. Singh (Eds.), Advanced Algorithmic Approaches to Medical Image Segmentation: State-of-the-Art Applications in Cardiology, Neurology, Mammography and Pathology, Springer, Berlin, 2002.

[7] M. Dulce, G. Mostbeck, Quantification of the Left Ventricular Volumes and Function with Cine MR Imaging: Comparison of Geometric Models with Three-Dimensional Data, Radiology 188 (371-376).

[8] S. Schalla, E. Nagel, H. Lehmkuhl, C. Klein, A. Bornstedt, B. Schnackenburg, U. Schneider, E. Fleck, Comparison of Magnetic Resonance Real-Time Imaging of Left Ventricular Function with Conventional Magnetic Resonance Imaging and Echocardiography, The American Journal of Cardiology 87 (1) (2001) 95–99.

[9] R. J. van der Geest, J. Reiber, Cardiovascular MRI and MRA, Lippincott,Williams and Wilkins, Philadelphia, 2003, Ch. 5, charles B. Higgins and Albert de Roos, editors.

[10] F. Frangi, et al., Three-Dimensional Modelling for Functional Analysis of Cardiac Images: A Review, IEEE Transations on Medical Imaging 20 (1).

[11] C. Comeau, Introduction to Cardiovascular MR Imaging, GE Medical Systems, GE Medical Systems, Milwaukee, Wisconsin (1999).
URL `http://www.gemedicalsystems.com/rad/mri/pdf/cardioapp.pdf`

[12] L. Bolinger, Magnetic Resonance Imaging, http://www.icaen.uiowa.edu/ bme186/lecturenotes/MRI.pdf (Dec 2002).

[13] S. G. Myerson, N. G. Bellenger, D. J. Pennell, Assessment of left ventricular mass by cardiovascular magnetic resonance, Hypertension 39 (2002) 750–755.

[14] Y. Ligier, O. Ratib, M. Logean, C. Girard, OSIRIS : A Medical Image Manipulation System, M.D. Computing Journal 11 (4) (1994) 212–218.

[15] J. Bosch, S. Mitchell, B. Lelieveldt, F. Nijland, O. Kamp, M. Sonka, J. Reiber, Automatic segmentation of echocardiographic sequences by active appearance motion models, IEEE Transactions on Medical Imaging 21 (11).

[16] S. C. Mitchell, B. P. Lelieveldt, J. G. Bosch, R. V. der Geest, J. H. Reiber, M. Sonka, Segmentation of Cardiac MR Volume Data using 3D Active Appearance Models, Proceedings of SPIE - The International Society for Optical Engineering 4684 I (2002) 433–443.

[17] P. Puech, L. Boussel, Dicomworks (1994).
URL `http://dicom.online.fr/`

[18] Y. Ligier, O. Ratib, M. Logean, C. Girard, Osiris : A medical image manipulation system, M.D. Computing Journal 11 (4) (1994) 212–218.
URL
`http://www.expasy.org/www/UIN/html1/projects/osiris/osiris.html`

[19] M. Urschler, H. Mayer, R. Bolter, F. Leberl, The LiveWire Approach for the Segmentation of Left Ventricle Electron-Beam CT Images, in: 26th Workshop of the Austrian Association for Pattern Recognition (AGM/AAPR), 2002, pp. 319–326.

[20] O. Gerard, T. Deschamps, M. Greff, L. Cohen, Real-time interactive path extraction with on-the-fly adaptation of the external forces, in: Proceedings of ECCV 2002, Copenhagen, Denmark, 2002.

[21] G. D. Waiter, et al., Determination of Normal Regional Left Ventricular Function from Cine-MR Images Using a Semi-Automated Edge Detection

Method, Magnetic Resonance Imaging 17 (1999) 99–107.

[22] J. Suri, Computer Vision, Pattern Recognition and Image Processing in Left Ventricle Segmentation: The Last 50 Years, Pattern Analysis and Applications 3 (3 2000) (2000) 209–242.

[23] L. P. Clarke, R. P. Velthuizen, M. A. Camacho, J. J. Heine, M. Vaidyanathan, L. O. Hall, R. W. Thatcher, M. L. Silbiger, Mri Segmentation: Methods and Applications, Magnetic Resonance Imaging 13 (3).

[24] D. L. Pham, C. Xu, J. L. Prince, A Survey of Current Methods in Medical Image Segmentation, Tech. rep., The John Hopkins University, The John Hopkins University, Baltimore, MD 21218 (Jan 1998).

[25] M. Kass, A. Witkin, D. Terzopoulos, Snakes: Active Contour Models, International Journal of Computer Vision 1 (4) (1988) 321–331.

[26] M. Santarelli, V. Positano, Automated cardiac MR image segmentation:Theory and Measurement Evaluation, Medical Engineering and Physics 25.

[27] L. Spreeuwers, M. Breeuwer, Detection of Left Ventricular Epi- and Endocardial Borders Using Coupled Active Contours, in: Computer Assisted Radiology and Surgery, 2003, pp. 1147–1152.

[28] R. W. A. Neubauer, A Skeleton-Based Inflation Model for Myocardium Segmentation, in: Proceedings of the 16th International Conference on Vision Interface, Halifax, Canada, 2003.
URL `http://kopernik.eos.uoguelph.ca/~zelek/vi2003/toc.html`

[29] T. McInerney, D. Terzopoulos, Deformable models in medical images analysis: A survey, Medical Image Analysis 1 (2) (1996) 91–108.

[30] S. Osher, J. A. Sethian, Fronts propagating with curvature-dependent speed: Algorithms based on Hamilton-Jacobi formulations, Journal of Computational Physics 79 (1988) 12–49.

[31] R. Malladi, J. A. Sethian, B. C. Vermuri, Shape modeling with front propagation: A level set approach, IEEE Transactions on Pattern Analysis and Machine Intelligence 17 (1995) 158–175.

[32] R. Malladi, J. A. Sethian, Level set methods for curvature flow, image enhancement, and shape recovery in medical images, in: Proc. of Conf. on Visualization and Mathematics, Berlin, Germany, 1997.

[33] J. A. Sethian, A marching level set method for monotonically advancing fronts, in: Proceedings of the National Academy of Sciences, Vol. 93, 1996.

[34] J. Montagnat, H. Delingette, A review of deformable surfaces: topology, geometry and deformation, Image and Vision Computing 19 (14) (2001) 1023–1040.

[35] L. H. Staib, J. S. Duncan, Boundary finding with parametrically deformable models, IEEE Transactions on Pattern Analysis and Machine Intelligence 14 (11) (1992) 1061–1075.

[36] T. McInerney, D. Terzopoulos, A dynamic finite element surface model for segmentation and tracking in multidimensional medical images with application to cardiac 4d image analysis, Computerized Medical Imaging and Graphics 19 (1) (1995) 69–83, special Issue on Cardiopulmonary Imaging.

[37] A. Chakraborty, L. H. Staib, J. S. Duncan, Deformable boundary finding in medical images by integrating gradient and region information, IEEE Transactions in Medical Imaging 15 (6) (1996) 859–870.

[38] T. F. Cootes, G. J. Edwards, C. J. Taylor, Active appearance models, Lecture Notes in Computer Science 1407 (1998) 484–498.

[39] G. Hamarneh, T. Gustavsson, Combining Snakes and Active Appearance Shape Models for Segmenting the Human Left Ventricle in Echocardiographic Images, IEEE:Computers in Cardiology 27 (2000) 115–118.

[40] M. Rogers, J. Graham, Robust Active Shape Model Search, in: Proceedings of the 7th European Conference on Computer Vision, 2002, pp. 517–530.

[41] M. B. Stegmann, Active Appearance Models:Theory, Extensions and Cases, Master's thesis, The Technical University of Denmark, Denmark (2000).

[42] S. C. Mitchell, B. P. F. Lelieveldt, R. J. van der Geest, H. G. Bosch, J. H. C. Reiber, M. Sonka, Multistage Hybrid Acive Appearance Model Matching: Segmentation of Left Ventricles in Cardiac MR Images, IEEE Transactions on Medical Imaging.

[43] B. P. F. Lelieveldt, S. C. Mitchell, J. G. Bosch, R. J. van der Geest, M. Sonka, J. H. C. Reiber, Quantification of Cardiac Ventricular Function using Magnetic Resonance Imaging (MRI) and Multi Slice Computed Tomography (MSCT), in: Proceedings on Information Processing in Medical Imaging, Davis, Ca, Usa, 2001, pp. 446–452.

[44] M. Lynch, O. Ghita, P. Whelan, Calculation of the Ejection Fraction from MR Cardio-Images, in: Proceedings of the Irish Machine Vision and Image Processing 2003, Coleraine, Co. Antrim, N. Ireland, 2003, pp. 9–17.

[45] A. Pednekar, Cardiac image analysis: Morphology, function and dynamics, Ph.D. thesis, University of Houston, Faculty of the Department of Computer Science, Prof. Ioannis A. Kakadiaris (December 2003).

[46] K. K. Delibasis, N. Mouravliansky, G. K. Matsopoulos, K. S. Nikita, A. Marsh, MR functional cardiac imaging: Segmentation, measurement and WWW based visualisation of 4D data, Future Generation Computer Systems 15 (2) (1999) 185–193.

[47] J. Suri, D. Wu, J. Gao, S. Singh, S. Laxminarayan, Comparison of state-of-the-art diffusion imaging techniques for smoothing medical/non-medical

image data, in: Proc. 15th International Conference on Pattern Recognition (ICPR'02), Quebec, 2002.

[48] G. Gerig, O. Kbler, R. Kikinis, F. Jolesz, Nonlinear anisotropic filtering of MRI data, IEEE Transactions on Medical Imaging 11 (2) (1992) 221–232.

[49] G. Sanchez-Ortiz, D. Rueckert, P. Burger, Knowledge-based tensor anisotropic diffusion of cardiac magnetic resonance images, Medical Image Analysis 3 (1).

[50] G. I. Sanchez-Ortiz, Fuzzy clustering driven anisotropic diffusion: Enhancement and segmentation of cardiac mr images, in: IEEE Nuclear Science Symposium and Medical Imaging Conference, Toronto, Canada, 1998.

[51] K. Chen, A Feature Preserving Adaptive Smoothing Method for Early Vision, Tech. rep., National Laboratory of Machine Perception and The Center for Information Science, Peking University, Beijing, China (1999).

[52] P. Perona, J. Malik, Scale-space and edge detection using anisotropic diffusion, IEEE Trans. on Pattern Analysis and Machine Intelligence 12 (7) (1990) 629–639.

[53] R. Duda, P. Hart, Pattern Classification and Scene Analysis, Wiley, NY, 1973.

[54] J. A. Hartigan, M. A. Wong, Statistical algorithms: Algorithm AS 136: A K-means clustering algorithm, Journal of Applied Statistics 28 (1) (1979) 100–108. URL `http://lib.stat.cmu.edu/apstat/136`

[55] Heart Rhythm Society, Patient and Public Information Center (2003). URL `http://www.naspe-patients.org/patients/ejection_fraction.html`

[56] J. Canny, A Computational Approach to Edge Detection, IEEE Transactions on Pattern Analysis and Machine Intelligence 8 (6) (1986) 679–698.

[57] H. Späth, Spline algorithms for curves and surfaces, Utilitas Mathematica Pub., 1974.

[58] J. Bland, D. Altman, Statiscal methods for assessing agreement between two methods of clinical measurements, Lancet 1 (8476) (1986) 307–310.

[59] M. Lynch, O. Ghita, P. F. Whelan, Extraction of epi-cardial contours from unseen images using a shape database, in: Proceedings of Nuclear Science Symposium and Medical Imaging Conference, NSS-MIC, 2004.

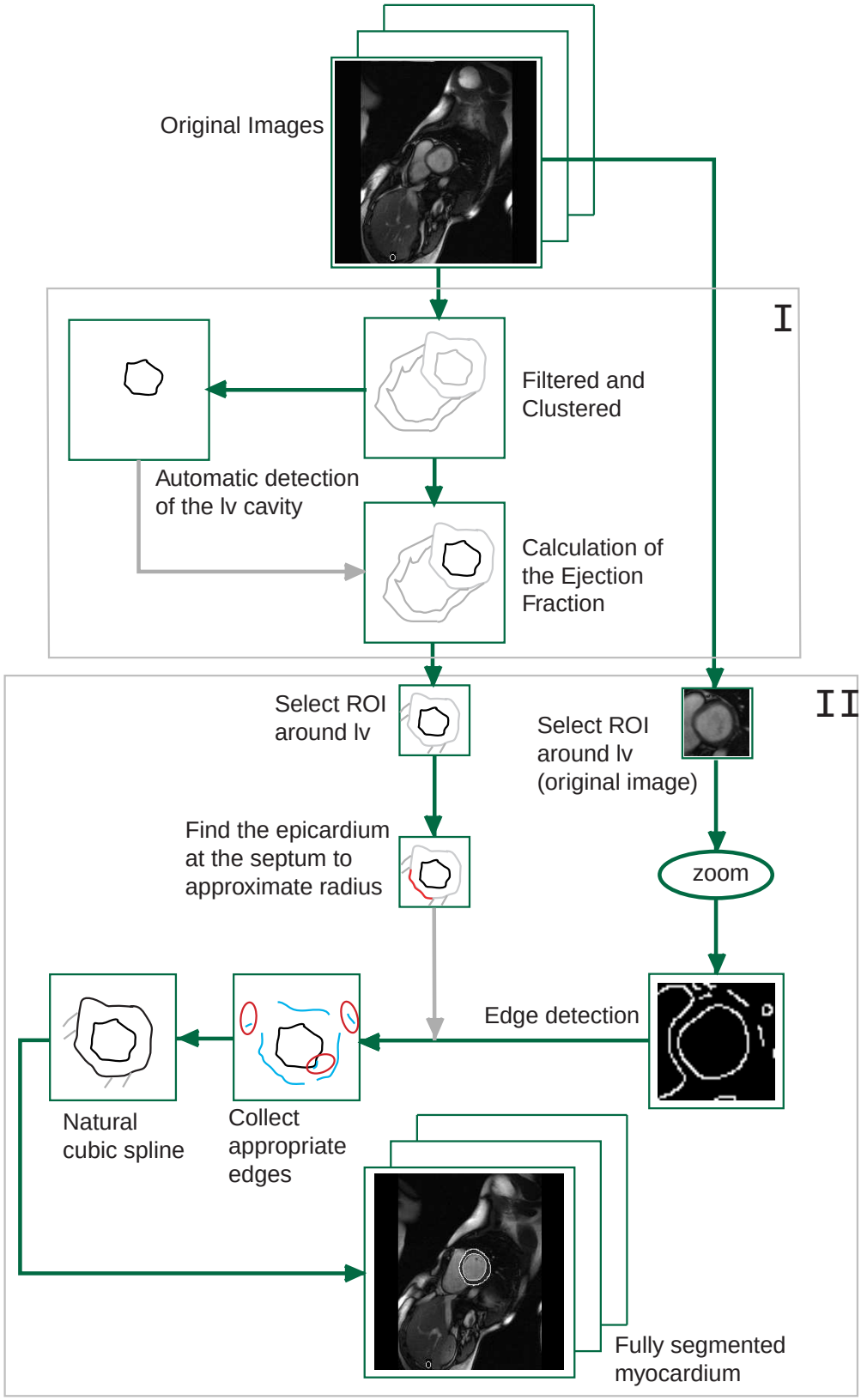

Fig. 4. A schematic representation of the two phases involved in the segmentation of the endo- and epi- cardium border. *Stage I* shows the preprocessing and segmentation processes, the automatic detection of the *lv* cavity and the connection of the cavity through the volume. *Stage II* shows the method for segmenting the epi-cardium border in each image

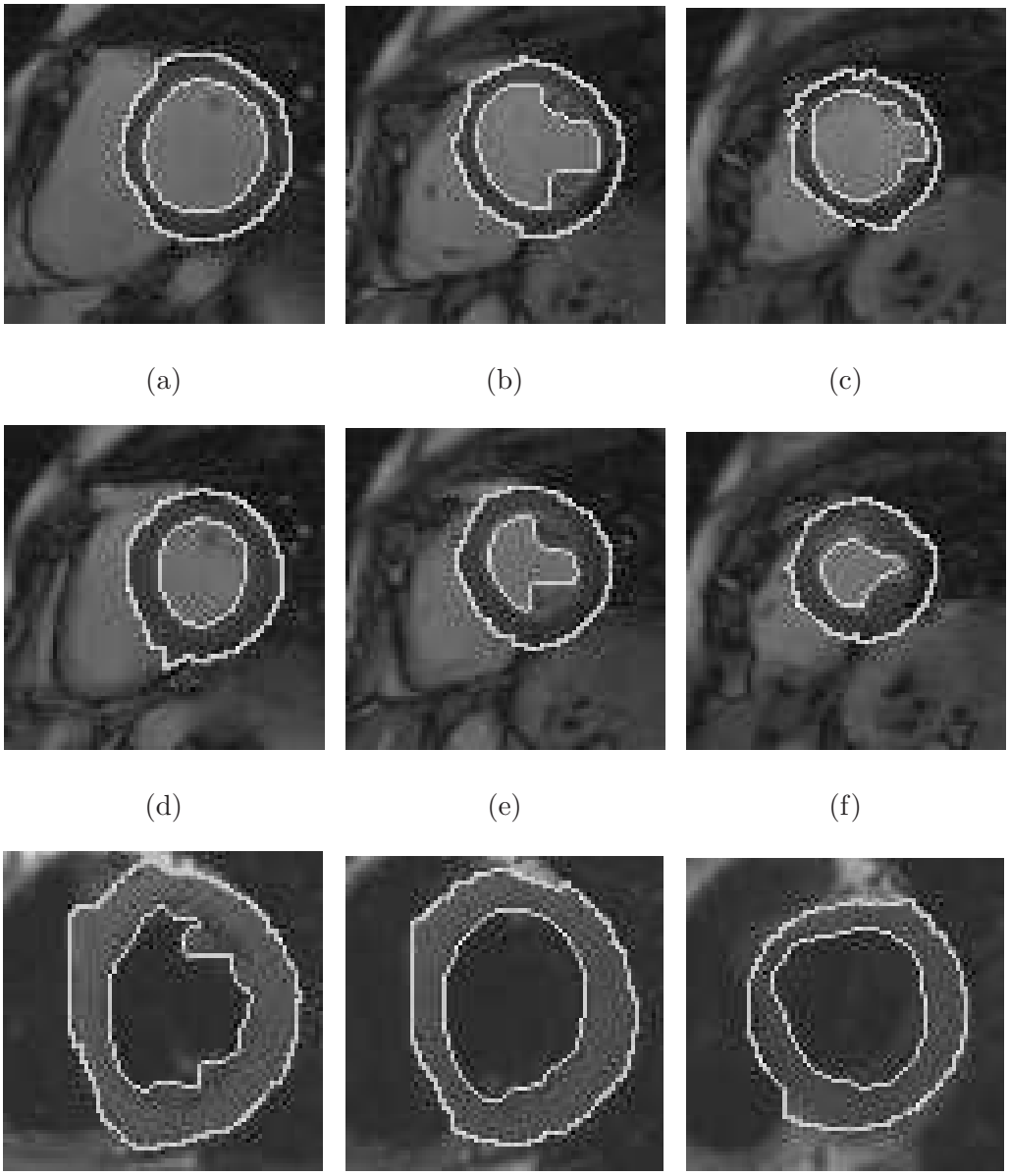

(a) (b) (c)

(d) (e) (f)

(g) (h) (i)

Fig. 5. The left ventricle contours obtained using our automatic segmentation method in short axis cardiac MR images. Figures (a)-(f) show images taken at both the end-diastolic phase and end-systolic phase of a gradient-echo sequence. Figures (g)-(i) show images from a spin-echo study.

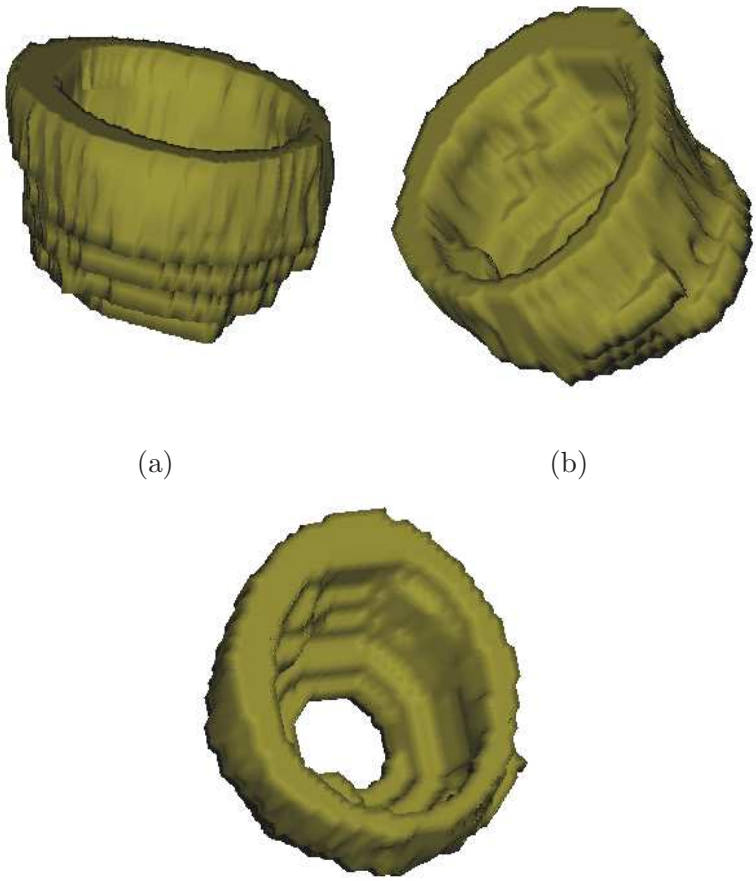

(a) (b)

(c)

Fig. 6. Figure shows the rendered myocardium for the end-diastolic phase

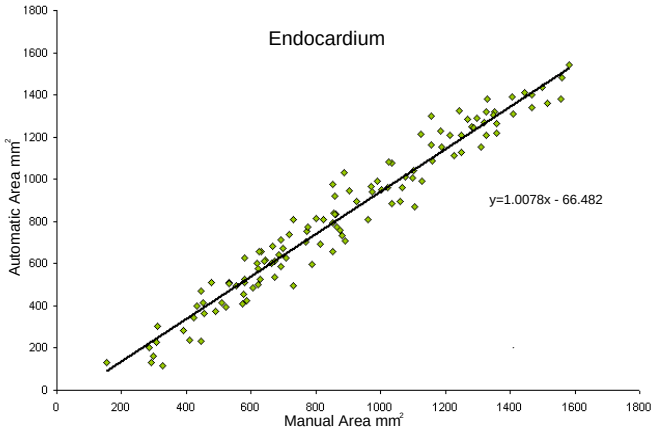

(a)

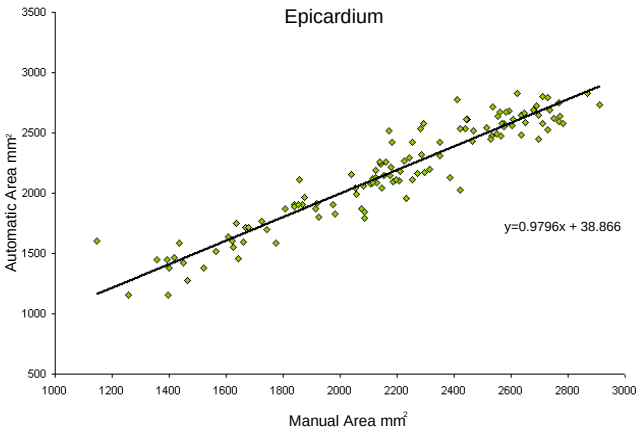

(b)

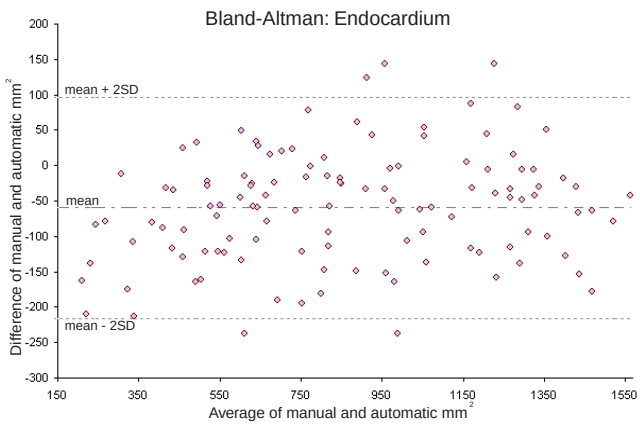

(c)

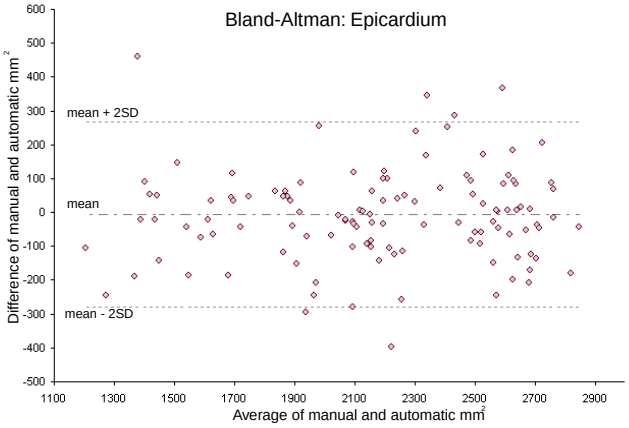

(d)

Fig. 7. Figures *(a)-(b)* shows scatterline plot of manual segmentation against the automatic segmentation for both the endo- and epi-areas and figures *(c)-(d)* shows Bland-Altman plot for the same

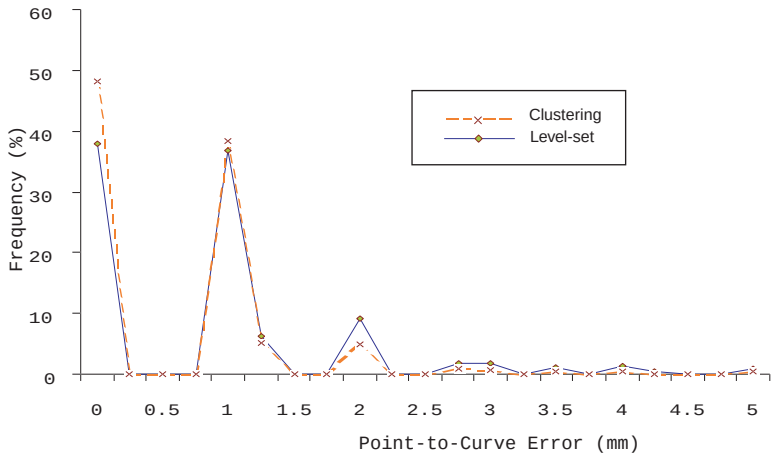

Fig. 8. Plot of the average thickness of the myocardium over 34 slices with both the manual segmentation and the automatic segmentation shown. Values are taken at evenly spaced radial positions around the endo cardium border.

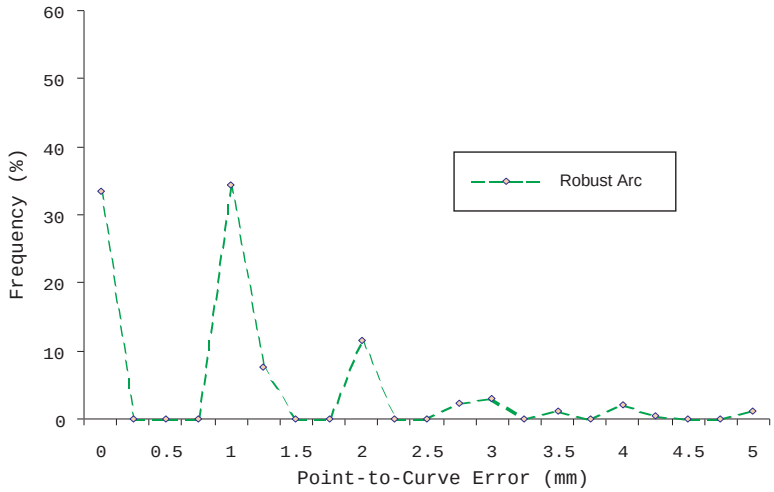

Fig. 9. Plot of the average thickness of the myocardium over 34 slices with both the manual segmentation and the automatic segmentation shown. Values are taken at evenly spaced radial positions around the endo cardium border.